This is the accepted manuscript made available via CHORUS. The article has been published as:

Multiple topologically nontrivial bands in noncentrosymmetric YSn_{2}

Yanglin Zhu, Tiantian Zhang, Jin Hu, Jamin Kidd, David Graf, Xin Gui, Weiwei Xie, Mengze Zhu, Xianglin Ke, Huibo Cao, Zhong Fang, Hongming Weng, and Zhiqiang Mao

Phys. Rev. B **98**, 035117 — Published 16 July 2018

DOI: 10.1103/PhysRevB.98.035117

Multiple topologically non-trivial bands in non-centrosymmetric YSn_2

Yanglin Zhu[1+], Tiantian Zhang[2+], Jin Hu[1,3,4*], Jamin Kidd[1], David Graf[5], Xin Gui[6], Weiwei Xie[6], Mengze Zhu[7], Xianglin Ke[7] , Huibo Cao[8], Zhong Fang[2], Hongming Weng[2]* and Zhiqiang Mao[1*]

[1] Physics and Engineering physics department, Tulane University, New Orleans, LA, 70118

[2]Beijing National Laboratory for condensed Matter Physics and Institute of Physics, Chinese Academy of Sciences, Beijing 100190, China

[3] Department of Physics, University of Arkansas, Fayetteville, AR, 72701

[4] Institute for Nanoscience and Engineering, University of Arkansas, Fayetteville, AR 72701

[5] National High Magnetic Field Laboratory, Tallahassee, FL 32310

[6] Department of Chemistry, Louisiana State University, Baton Rouge LA 70803

[7] Department of Physics and Astronomy, Michigan State University, East Lansing, MI 48824-2320

[8] Quantum Condensed Matter Division, Oak Ridge National Laboratory, TN 37831, USA.

Abstract

The square lattices formed by main-group elements such as Bi, Sb, Sn and Si in layered materials have attracted a lot of interest, since they can create rich topological phases. In this article, we report the slightly distorted square lattice of Sn in a non-centrosymmetric compound YSn_2 generates multiple topologically non-trivial bands, one of which likely hosts nodal line and tunable Weyl semimetal state induced by the Rashba spin-orbit coupling (SOC) and proper external magnetic field. The quasiparticles described as relativistic fermions from these bands

are manifested by nearly zero mass and non-trivial Berry phases probed in de Haas–van Alphen (dHvA) oscillations. The dHvA study also reveals YSn_2 has a complicated Fermi surface (FS), consisting of several 3D and one 2D pockets. Our first principle calculations show the point-like 3D pocket at Y point on the Brillouin zone boundary hosts the possible Weyl state. Our findings establish YSn_2 as a new interesting platform for observing novel topological phases and studying their underlying physics.

YLZ and TTZ equally contributed to this work

* jhu@tulane.edu; hmweng@iphy.ac.cn; zmao@tulane.edu

I. INTRODUCTION

Three-dimensional (3D) topological Dirac and Weyl semimetals are characterized by linear band crossings near the Fermi level. The low energy excitation around the Dirac or Weyl nodal points are viewed as quasiparticles or emergent relativistic fermions, which can be described by Dirac/Weyl equation. These relativistic fermions result in exotic properties of the host materials, such as large magnetoresistance [1], high carrier mobility [1,2] and chiral anomaly [3]. The 3D Dirac semimetals (DSMs) were first predicted and then discovered in Na_3Bi [4,5] and Cd_3As_2 [6–8], which show four-fold degenerate Dirac nodes. When the spin degeneracy is lifted by breaking time reversal symmetry or inversion symmetry, a Dirac semimetal is expected to evolve into a Weyl semimetal (WSM), with each Dirac cone splitting into a pair of Weyl cones with opposite chirality [9,10]. The inversion symmetry breaking WSM state was first realized in transition metal monopnictides (Ta/Nb)(P/As) [9–16] and photonic crystal [17], and even extended to phononic crystal [18]. The time reversal symmetry breaking Weyl state has been predicted in many material systems such as $Y_2Ir_2O_7$ [19], $HgCr_2Se_4$ [20], $YbMnBi_2$ [21] and Heusler compounds Co_2XZ(X=IVB or VB, Z=IVA or IIIA) [22,23] and most of these predictions are still awaiting for experimental verifications. Additionally, a new type (type-II) of Weyl nodes violating the Lorentz symmetry has recently been reported in several material systems including WTe_2 [24,25], $MoTe_2$ [26,27], LaAlGe [28] and TaIrTe4 [29–32]; such a type-II Weyl state features strongly tilted Weyl cones, which lead to the touching of the electron and hole Fermi pockets at Weyl points.

Recently, there has been growing interest in relativistic fermions generated by 2D square lattices. Several material families with square lattices have been found to harbor relativistic

fermions, including $AMnBi_2$ (A=Ca, Sr, Ba, or rare earth element) [21,33–36], $AMnSb_2$ (A=Ca, Sr, Ba, or rare earth element) [37–42], and *WHM* (*W* = Zr, Hf, or rare earth elements; *H* = Si, Ge, Sn, Sb; and *M* = S, Se, Te) [43–52] – type compounds. The 2D square lattices consisting of group IV or V elements such as Si, Sn, Ge, Bi and Sb play a critical role in generating relativistic fermions in these materials. Such a 2D square lattice effectively forms check-board like complex lattice due to its chemical environment. This might result in band-folding and nonsymmorphic symmetric operation, which are closely related with band topology. A rich variety of topological phases have been observed or predicted in these materials, e.g. the anisotropic Dirac cone state [33], the nodal-line state [44,46,53], the 2D non-symmorphic Dirac state [44], time-reversal symmetry breaking Weyl state [21,38], quantum spin Hall insulator in ZrSiO monolayer [43], etc. This suggests that layered compounds with the square lattices formed by group IV/V elements are fertile ground for the search of new topological phases. Here, we report the discovery of a new layered topological semimetal YSn_2 with a non-centrosymmetric crystal structure and lightly distorted Sn square lattice. We find this material possesses multiple topologically non-trivial bands, one of which hosts a new type of tunable Weyl state induced by Rashba spin-orbit coupling (SOC) and tunable by magnetic field.

II. METHODS

A. Experiment

The YSn_2 single crystals used in this study were synthesized using a flux method. The Y pieces and Sn lumps with molar ratio of 1:4 were loaded in an Al_2O_3 crucible and sealed in a quartz tube under high vacuum. The mixtures were then heated to 1050 °C and held at this temperature for 48 hours for homogeneously melting, followed by a slow cooling down to

750 °C at rate of 2 °C per hour and then a quick cooling down (4°C/h) from 750 °C to 350 °C. Excessive Sn flux was removed by centrifugation. The excellent crystallization of the single crystals was confirmed by the sharp (0 *K* 0) X-ray diffraction (XRD) peaks, as shown in Fig. 1d. The inset in Fig. 1d displays an optical image of a typical YSn_2 crystal. We have also measured the composition of the synthesized crystals using energy dispersive X-ray spectrometer (EDS) and the measured composition is $YSn_{1.95}$, slightly deviated from the expected stoichiometric composition YSn_2. The Sn deficiency implies that there are possible vacancies at Sn sites. The magnetization was measured using a SQUID magnetometer (Quantum Design) and the magnetic torque measurements were carried out at the NHMFL in Tallahassee using a cantilever torque magnetometer.

We have studied the structure of YSn_2 using both single crystal neutron and X-ray diffractions. Neutron diffraction measurements were performed at room temperature using the HB-3A four-circle diffractometer (λ=1.003 Å) at High Flux Isotope Reactor in Oak Ridge National Laboratory. The crystal structure of YSn_2 was obtained via Rietveld refinement of a collection of nuclear Bragg peaks using the FullProf program, as described in supplementary Table S1. For the X-ray diffraction (XRD) measurements, the YSn_2 single crystal sample was mounted on the tips of Kapton loop. Room temperature (293K) intensity data were collected on a Bruker Apex II X-ray diffractometer with Mo radiation $K\alpha_1$ (λ=0.71073 Å) using a completely identical sequence. Data were collected over a full sphere of reciprocal space with 0.5° scans in ω with an exposure time of 10s per frame. The 2θ range extended from 4° to 75°. The SMART software was used for data acquisition. Intensities were extracted and corrected for Lorentz and polarization effects with the SAINT program. Numerical absorption

corrections were accomplished with XPREP which is based on face-indexed absorption [54].The twin unit cell was tested. With the SHELXTL package, the crystal structures were solved using direct methods and refined by full-matrix least-squares on F^2 [55].

B. Computation

The first principle calculation for YSn_2 is based on density functional theory (DFT) [56,57] within the Perdew-Burke-Ernzerhof (PBE) exchange-correlation [58,59] implemented in the Vienna *Ab initio* Simulation Package [60,61]. The plane-wave cutoff energy is 520eV with a $8\times8\times12$ *k*-mesh in the Brillouin zone (BZ) [62]. We employ maximally localized Wannier functions [63,64] to obtain the tight-binding model of the bulk YSn_2 and use it for the Fermi surface (FS) calculation.

III. RESULTS AND DISCUSSIONS

A. Structure determination of YSn_2

Previous powder XRD studies show YSn_2 possesses an orthorhombic structure with space group *Cmcm* [65,66]. Although our neutron scattering spectra can be refined by the reported centrosymmetric *Cmcm* crystal structure, we found that two slightly different non-centrosymmetric orthorhombic structures with space groups *C2cm* and $Cmc2_1$ can also yield good refinements. As shown in Supplementary Table S1, the agreement factors are comparable among these three refinements, which prevent us from determining the exact structure of YSn_2. Since these three different space groups correspond to the same powder diffraction pattern, it is difficult to determine whether the structure has inversion symmetry or not through powder

diffraction spectra refinements. This inspired us to determine if our synthesized YSn_2 has broken inversion symmetry through single crystal XRD measurements. We conducted careful single crystal XRD measurements on YSn_2 and refined the structure with different space groups. We find that the best refinement is obtained with the space group *Cmc2₁*. The flack factor obtained in this refinement is 0.3(2), which confirms the non-centrosymmetric structure. Supplementary Table S2 and S3 present the comparison of crystallographic data between $Cmc2_1$ and *Cmcm*. The $Cmc2_1$ structure of YSn_2 is also supported by our first principle calculations which show that only the band structure calculated with the space group of $Cmc2_1$ matches with the experimentally probed bands (see below).

Fig. 1a depicts the crystal structure of YSn_2 determined by our XRD experiment, which can be viewed as the alternative stacking of the Sn staggered layers and the Sn planes, with Y ions located in between. As shown in Fig. 1b, the Sn planar layer is a distorted square net with the bonding angles slightly deviating from 90°. It is worth noting that the two bonding angles shown in Fig. 1b are not supplementary (i.e., not adding up to 180 degrees), indicating that this plane is not exactly 2D. That is, the Sn layers are slightly corrugated along the *a*- or *c*-axis, as shown in Fig. 1c.

B. Relativistic fermion behavior probed by dHvA oscillations in YSn_2

Signatures of topological relativistic fermions in YSn_2, including light effective mass, high mobility, and nontrivial Berry phase, have been found from our quantum oscillation studies on YSn_2 single crystal samples. We have observed clear dHvA oscillations in the isothermal

magnetization measured using a SQUID magnetometer. As shown in Fig. 2a, when the magnetic field was applied along the out-of-plane direction (i.e., B//b-axis), the magnetization at 1.8 K starts to oscillate for $B > 3.2$ T and the oscillations remain observable up to 21 K. The oscillations look more striking after removing the background, as shown in Fig. 2b. The Fast Fourier transform (FFT) analyses show such dHvA oscillations consist of a single oscillation frequency of $F_\beta = 78$ T, as shown in the inset to Fig. 2c. For the in-plane magnetic field, no oscillations were probed up to 7 T (the highest field of the SQUID). However, as will be presented later, we observed multi-frequency dHvA oscillations for both out-of-plane and in-plane magnetic fields in high field magnetic torque measurements. The observation of low-field dHvA oscillations in the magnetization measured using a SQUID is rare and its presence usually implies high carrier mobility.

The relativistic fermion properties of YSn_2 were found from the analyses of the observed dHvA oscillations. In general, the dHvA oscillations of a topological material can be described by the Lifshitz-Kosevich (LK) formula [67,68] with a Berry phase being taken into account [69]:

$$\Delta M \propto -B^{1/2} R_T R_D R_S \sin[2\pi(\frac{F}{B} + \gamma - \delta)] \qquad (1),$$

where $R_T = \alpha T m^*/[Bm_0 \sinh(\alpha T m^*/Bm_0)]$, $R_D = \exp(-\alpha T_D m^*/Bm_0)$ and $R_S = \cos(\pi g m^*/2m_0)$. T_D is the Dingle temperature, and $\alpha = (2\pi^2 k_B m_0)/(\hbar e)$. The oscillations of ΔM is described by the sine term with a phase factor $\gamma - \delta$, in which $\gamma = \frac{1}{2} - \frac{\phi_B}{2\pi}$ and ϕ_B is Berry phase. The phase shift δ, which is determined by the dimensionality of the FS, is 0 and $\pm 1/8$ respectively for 2D and 3D cases. For the 3D case, the sign of δ depends on whether the probed extreme cross-section area

of the FS is maximal or minimal. δ = -1/8 (1/8) for maximal (minimal) cross-section for a 3D electron pocket and vice versa for a 3D hole pocket [68].

From the LK formula, the effective mass m^* can be obtained through the fit of the temperature dependence of the oscillation amplitude to the thermal damping factor R_T. As shown in Fig. 2c, the effective masses we obtained from this type of fit for the observed dHvA oscillation of magnetization is $(0.082\pm0.002)m_0$ where m_0 is the free-electron mass. Since the FFT amplitude (FFTA) is used as the oscillation amplitude for the fit in Fig. 2c, the inverse field $1/B$ in R_T should be replaced by the average inverse field $1/\overline{B}$, defined as $1/\overline{B} = (1/B_{max} + 1/B_{min})/2$, where B_{max} and B_{min} define the magnetic field range used for the FFT. With the effective masses and the oscillation frequency being the known parameters, we have further fitted the dHvA oscillation pattern at 1.8 K by the LK-formula (Eq. 1), as shown in Fig. 2d. Such an oscillation pattern fit yields the Dingle temperature of 10K, from which the quantum mobility μ_q [$= e\hbar/(m^* 2\pi k_B T_D)$] is estimated to be 2609 $cm^2V^{-1}s^{-1}$.

The relativistic nature of carriers in YSn_2 is supported by the non-trivial Berry phases. The phase factors of the oscillations extracted from the above LK-fit (Fig. 2d) is $\gamma - \delta$ = 0.01, from which the Berry phase of $(0.49-\delta) \times 2\pi$ can be derived. As will be shown below, the Fermi pocket associated with the F_β =78 T frequency displays 2D characteristics, implying that δ should be taken as 0 for the F_β band. Thus, the Berry phase is 0.98π, close to the ideal value of π for Dirac-like energy band crossings.

The observation of single frequency dHvA oscillation in the low field range does not necessarily imply YSn_2 is a single band system. In order to gain more insights into its electronic band structure, we have further extended the dHvA studies to high fields up to 31 T, through the magnetic torque measurements [which were performed at the National High Magnetic Field Lab (NHMFL), Tallahassee]. We observed multiple oscillation frequencies in these measurements, implying that YSn_2 has a complicated Fermi surface. In Fig. 3a, we present the torque oscillation pattern measured with the field applied nearly along the out-of-plane direction (denoted as $B//b'$). We chose such a field orientation is because that the torque signal vanishes when the field is perfectly aligned normal or parallel to the surface of the cantilever tip [47]. The dHvA oscillations under high magnetic fields show multiple frequencies. As shown in the Fig. 3b, three major frequencies can be resolved in the FFT spectrum, i.e., F_α = 23T, F_γ = 301T and F_θ = 433T. These frequencies originate from three different 3D Fermi pockets according to the first principle calculations (see below). Surprisingly, the oscillation frequency of F_β =78T seen in the low field magnetization measurements (Fig. 2c, inset) is not probed in torque. This is possibly due to the fact that the torque signal is the weakest for the out-of-plane or in-plane field. This conjecture is verified by the observation that the F_β oscillation component appears when the field is tilted away from the out-of-plane direction. The effective quasi-particle masses m^* corresponding to F_α, F_γ, and F_θ probed in torque are estimated to be $(0.029\pm0.002)m_0$ (m_α^*), $(0.023\pm0.002)m_0$ (m_γ^*) and $(0.038 \pm 0.004)m_0$ (m_θ^*). The fits of the temperature dependences of the FFT amplitudes from which m^* is derived are shown in Fig. 3c.

Although m_α^*, m_γ^* and m_θ^* are comparable and F_α is one order of magnitude smaller than F_γ or F_θ, the FFT amplitude of F_α is about 16 times stronger than that of F_γ or F_θ, as shown

in Fig. 3b, which implies that the quasi-particles hosted by the F_α pocket must have much longer life time (i.e., higher quantum mobility) compared with the F_γ or F_θ pocket. To further evaluate the quasi-particle properties of the F_α pocket, we have performed the LK-fit for the T = 1.7K oscillatory torque obtained by subtracting the non-oscillating background. To minimize fitting parameters, we have filtered the F_γ and F_θ components and the fit is made for the single F_α component, as shown in Fig. 4a. This LK fit yields a quantum mobility of 776 cm^2/Vs and a Berry phase of $(0.309 - \delta)\times 2\pi = 0.968\pi$, suggesting non-trivial band topology. Here we take $\delta = -1/8$, since the F_α pocket is a 3D sphere-like electron pocket as discussed below and the probed F_α oscillation should correspond to a maximal cross-section of the F_α pocket for $B//b'$. The first principle calculations find that around the F_α pocket the related two bands can host nodal line and such a nodal line decays into a Weyl semimetal state caused by Rashba spin-orbit coupling and proper external magnetic field, which will be discussed in great details below. On considering the very small mass, high mobility and closeness to both nodal line and WSM state, the F_α pocket is most probably topologically nontrivial. For the high frequency oscillation components F_γ and F_θ, however, their LK fits are difficult since their dHvA oscillations show a low signal-to-noise ratio.

In order to further characterize the properties of the quasi-particles hosted by the F_α-, F_γ-, and F_θ-pockets, we have also performed high-field magnetic torque measurements with the field applied nearly along the in-plane direction (denoted as $B//ac'$). Strong dHvA oscillations have also been observed in these measurements, as shown in Fig. 3d. The FFT analyses of these data (Fig. 3e) reveal four major fundamental frequencies, i.e., 21T, 386T, 465T and 655T. The first three frequencies correspond, respectively, to F_α, F_γ and F_θ probed with $B//b'$ and such a

correspondence is manifested by the angular dependences of the oscillation frequencies, which will be presented below. However, the highest frequency 655T (denoted by F_ϕ) is an additional component, which is not probed for $B//b'$. From the fit of temperature dependence of FFT amplitude, we have also estimated m^* for each oscillation frequency probed for $B//ac'$ (Fig. 3f) and found m^* is also very small for all probed frequencies and within the range of (0.022-0.065)m_0, consistent with the small values of m^* [~ (0.023-0.038)m_0] probed with $B//b'$. Table II lists m^* for all frequencies probed in both field orientations for comparison. The errors of the fitted m^* are also given in this table. As will be shown later, these experimentally measured m^* agrees well with the first principle calculated mass (Table III).

For the dHvA oscillations shown in Fig. 3d, we have also conducted Berry phase analyses. In general, for multiple frequency quantum oscillations, the Berry phase for each band can be extracted via fitting the oscillation pattern by a multi-band LK model which can be generalized from Eq. (1) [70,71]. In order to achieve more accurate fits, we have separated the low (F_α=21 T)- and high (F_γ=386 T and F_θ=465 T)-frequency oscillation components and fit them individually, as shown in Figs. 4b and 4c. The F_ϕ- component has been filtered out, since this component exhibits very few oscillation peaks in the measured field range, which hinders a meaningful fit. As shown in Fig. 4b, for the F_α component, the oscillation becomes aperiodic above 14T, which is most likely due to Zeeman effect and cannot be fitted by the simple LK-formula with only the fundamental frequency (Eq. 1). Therefore, our fit for this component is performed within the < 14T field range. For the high frequency components (F_γ and F_θ) shown in Fig. 4c, the two-band LK model can well reproduce the oscillation pattern at T=1.7 K. From these LK-fits, we also obtained non-trivial Berry phases not only for the F_α-pocket, but also for

the F_γ-, and F_θ-pockets, as listed in Table II [Note that δ should be taken as 1/8 for the F_α-pocket for $B//ac'$, since the Rashba effect splits this Fermi surface, leading to a minimum cross section for $B//ac'$ (see below)]. This indicates that all the F_α-, F_γ-, and F_θ-pockets host relativistic fermions. Other signatures of relativistic fermions such as high quantum mobility and small effective mass are also revealed from the above LK fits, as summarized in Table II. The LK mass fits for F_α, F_γ, F_θ and F_ϕ for $B//ac'$ are shown in Fig. 3f. The F_α-pocket, while being the smallest, host relativistic fermions with much higher quantum mobility (~1621 $cm^2V^{-1}s^{-1}$ for $B//ac'$, almost twice of those of the F_γ-, and F_θ-pockets). High quantum mobility generally means low back-scattering rate in cyclotron motions. This might be the reason why the FFT amplitude of the F_α-pocket is much stronger than those of the F_γ-, and F_θ-pockets (Fig. 3b and 3e). These facts imply that the relativistic fermions of the F_α-pocket may have better topological protection against back-scattering than those of the F_γ-, and F_θ-pockets. As will be shown below, the F_α-pocket is at the Y point on the Brillouin zone boundary and hosts a Weyl state driven by Rashba spin-orbital coupling.

In addition to the quantum oscillation studies for $B//b'$ and $B//ac'$, we have also measured the angular dependence of the dHvA oscillations to reveal the information on the Fermi surface morphology. With the field being rotated from the out-of-plane ($B//b$, defined as $\theta = 0°$) to the in-plane ($B//ac$, $\theta = 90°$) direction (see the inset of Fig. 5c for the experiment setup), the dHvA oscillations probed in both the low-field magnetization (Fig. 5a) and the high field torque (Fig. 5b) display clear evolutions. The backgrounds have been subtracted for the dHvA oscillation data presented in Fig. 5a and 5b. The dHvA oscillations in magnetization show only a single

frequency F_β in the low angle range of < 30°, but double frequencies for 30° < θ < 45°, i.e., F_β and an additional low frequency. The low additional frequency component (displayed by white open circles in Fig. 5c) is actually the F_α component detected in the torque measurements. As noted above, the oscillation frequency of F_β is absent in the torque measurements for the field exactly along the *b*-axis, but it appears when the field is tilted away from the *b*-axis. In both the magnetization and torque measurements, the F_β oscillation component was found to disappear when θ is increased above 45°. As seen in Fig. 5c, F_α as well as F_β probed by both techniques are consistent. The fact that F_β is present only for $\theta < 45°$ and its angular dependence $F_\beta(\theta)$ follows the $1/\cos\theta$ dependence (see the red fit curve in Fig. 5c) suggests the existence of a small 2D Fermi pocket, which is expected for a layered material like YSn_2. For other frequencies, F_α, F_γ, F_θ, and F_ϕ, their angular dependences all display 3D characters. Particularly, F_α is almost independent of angle, suggesting a very small, sphere-like Fermi surface, which is consistent with the calculated Fermi surface as shown in the next section.

It is interesting to note that although the F_α-band hosts a Weyl state as discussed below, the quantum mobility of the relativistic fermions hosted by this band (776 $cm^2V^{-1}s^{-1}$ for $B//b'$) is smaller than that of the F_β-band (2609 $cm^2V^{-1}s^{-1}$). This may be associated with the fact that the F_α- and F_β-bands form two different Fermi surfaces with different morphology, dimensionality and Fermi velocity. Given quantum oscillations originate from cyclotron motions, the scattering process could be very different between the F_α- and F_β-pockets due to their different Fermi surface properties. Unlike transport mobility, which is only sensitive to large angle scattering, the quantum mobility depends sensitively on both small and large angle scattering. As a result, it is

not surprising to see different quantum mobility between two non-trivial pockets with different Fermi surfaces. The other possibility is that the F_β band may host a new topological state, which may have better topological protection against scattering than the F_α band. Clarification of this matter requires further studies.

C. Electronic band structure of YSn_2

In order to understand the relativistic fermion behavior revealed through the dHvA studies on YSn_2, we performed first-principles calculation for both the $Cmc2_1$ and $Cmcm$ crystal structures and found that the band structure calculated with the space group of $Cmc2_1$ is nearly consistent with the bands probed by the dHvA experiments, while the band structure of $Cmcm$ does not match with the experimentally-probed bands at all. Figs. 6 and 7 display the calculated band structure and FS respectively for the $Cmc2_1$ structure (the band structure and FS calculated with the space group of $Cmcm$ is shown in Supplementary in Fig. S1). These calculated results clearly show YSn_2 is a multiple band system. Its Fermi surface consists of multiple sheets as shown in Fig. 7a-7c. The energy bands probed in the dHvA calculations mostly agree with calculated ones. Specifically, three calculated small pockets, i.e., the α-, γ- and θ-pockets (see Fig. 7b and 7c for the α- and γ-pockets) all have been probed in the dHvA oscillations. As shown in Table III, the calculated Fermi wave vectors k_F as well as the effective quasi-particle mass for these three pockets are in good agreement with those derived from the F_α, F_γ and F_θ oscillation components. Fig. 7d and 7e show the FS at $k_y = 0$ and π respectively, from which we can see the α-pocket is at the highly symmetric momentum point, i.e., the Y point on the BZ boundary, while the γ- and θ-pockets are at accidental momentum points (see Fig. 6b-6d). The calculated α-,

γ- and θ-pockets all exhibit 3D characters, consistent with the angular dependences of F_α, F_γ and F_θ shown in Fig. 5c. The estimated k_F given in Table III for the α-, γ- and θ-pockets are based on the cross sections of these pockets at the $k_y = 0$ and π planes (Fig. 7d and 7e). The calculations also reveal several other bigger Fermi pockets shown in Fig. 7a-7c. However, these pockets were not clearly resolved in the dHvA oscillations possibly due to the lower mobility of quasi-particles hosted by these pockets. Since these pockets have very complex morphologies, it is hard to tell whether the F_ϕ -band is associated with them. As indicated above, in the dHvA oscillations, we have also probed a 2D band hosting relativistic fermions in the dHvA oscillations, i.e. the F_β band, but this band is not clearly reflected in the calculated band structure.

Next, we will show the α-pocket hosts a Weyl semimetal state driven by the Rashba SOC coupling and external magnetic field. Glide mirror $\bar{M}_y\left\{\frac{1}{2},\frac{1}{2},0\right\}$ (Fig. 6a) and time-reversal symmetry τ play import roles in YSn_2. Here, we define an antiunitary symmetry Θ as their composition. $\Theta = \bar{M}_y * \tau$. Importantly, $\Theta^2 = \bar{M}_y{}^2 * \tau^2 = T_{110} = e^{-i(k_x a + k_y b)}$, where k_x and k_y are reciprocal lattice vectors, a and b are crystal constants, and T_{110} is the unit lattice translation along the (110) direction. Specially, we will get Kramers degeneracy $\Theta^2 = -1$ at the BZ boundary where $k_x = 0$， $k_y = \pi/b$. Thus, the green dashed lines (T–Y) in Fig. 7f will be double-degenerate, forming a nodal line in the BZ. However, since the space group $Cmc2_1$ has no inversion symmetry and a polar axis is allowed along the z direction, the Rashba type spin-orbit coupling will break the degeneracy along the directions other than T-Y on the $k_y = \pi/b$ plane. So the α-pocket is spin splitting other than the two red dots shown in Fig. 7g where it intersects with the

nodal line along T-Y. The Rashba like effective Hamiltonian at the $k_y = \pi/b$ plane is $H_R = \sigma_z k_x - \sigma_x k_z$ without considering other symmetries in YSn_2. Once an external magnetic field, e.g. B_z, is applied in the *ac* plane to the system, such Rashba term will become to $H_R' = \sigma_z(k_x + B_z) - \sigma_x k_z$ and time-reversal symmetry will be broken. Therefore, on one hand, the 2-fold degenerate nodal line along T-Y will decay into Weyl points due to the Θ symmetry breaking; on the other hand, such Weyl points will move along the direction perpendicular to the magnetic field to ($-Bz$, π/b, 0). Once the Weyl points are achieved around the Fermi energy, they can lead to a π Berry phase for electrons making cyclotron motion on the α-pocket, as demonstrated in the dHvA experiments discussed above. For an external magnetic field along the b' direction, Zeeman splitting introduces tiny band gap around Y and along the nodal line T-Y, which leads to small deviation of Berry phase from π proportional to the size of gap [72]. Insets (i), (ii), (ii) and (iv) in Fig. 7g depict four possible paths of cyclotron motion for electrons in the α-pocket. However, the slight difference in the cyclotron frequency is not resolved in present dHvA experiments due to the quite small Rashba splitting and limited experimental resolution.

As seen in Fig. 6c, the Rashba spin splitting (RSS) energy for YSn_2 is about 3.6 meV, which is much smaller than that of a typical Rashba semiconductor BiTeI whose RSS reaches 400 meV [73]. However, as long as the RSS energy is larger than the Zeeman energy, a non-trivial Berry phase is expected for the Weyl node induced by the RSS as discussed above, but a deal Berry phase of π is expected only when the RSS energy is much larger than the Zeeman energy. The dHvA oscillations probed in torque measurements indeed suggest that the RSS energy of the α-pocket is much greater or greater than the Zeeman energy. For $B//ac'$, we find that the dHvA oscillations of the α-pocket start to deviate from the LK fit from 14T, which is

most likely caused by the Zeeman effect (Fig. 4b). The Zeeman energy at 14T is ~0.8 meV, indicating the Zeeman energy in the field range of <14T is smaller than the RSS energy. For $B//b'$, the Zeeman effect is much weaker, we do not observe clear trace of Zeeman splitting and the dHvA oscillation pattern can be fitted by the LK formula in the whole field range (see Fig. 4a). The experimental observation of non-trivial Berry phase for both field configurations for the α-pocket (i.e. $\phi_B = 0.968\pi$ for $B//b'$ and 0.87π for $B//ac'$) provides a strong support for our prediction that weak Rashba effect can create a Weyl node at Y point in YSn_2.

IV. CONCLUSION

In summary, we have synthesized single crystals of YSn_2 and characterized its crystal structure using neutron scattering and single crystal XRD. Although previous work suggested YSn_2 has an orthorhombic centrosymmetric structure with space group of *Cmcm*, we find our YSn_2 single crystals possess a non-centrosymmetric $Cmc2_1$ structure. We also performed quantum oscillation studies on this compound through magnetization and magnetic torque measurements, from which we have demonstrated that it has multiple bands hosting relativistic fermions, including several 3D bands and one 2D band. From first principle calculations, we found one of the 3D bands hosts a new type of Weyl state caused by Rashba spin-orbital coupling. This band forms a point-like FS at Y point on the BZ boundary. Other 3D bands probed in the dHvA oscillations have also been predicted in the band structure calculations. However, the 2D band seen in the experiment was not revealed in the calculations, which is yet to be studied. Our findings show YSn_2 is an interesting playground for observing and understanding novel topological phases. In addition, given that YSn_2 belongs to a large family of material $RESn_2$ (RE = rare earth), our results may motivate further studies on other isostructural

$RESn_2$ compounds which show magnetic orders. If they also harbor relativistic fermions, they may provide opportunities to study the interplay between relativistic fermions and magnetism.

ACKNOWLEDGEMENTS

This work was supported by the US Department of Energy (DOE) under Grant No. DE-SC0014208. A portion of this work was performed at the National High Magnetic Field Laboratory, which is supported by National Science Foundation Cooperative Agreement No. DMR-1157490 and the State of Florida. The band structure calculation work was supported by the National Key Research and Development Program of China (Grant No. 2016YFA0300600), the National Natural Science Foundation of China (Grant No. 11674369), and the “Strategic Priority Research Program (B)" of the Chinese Academy of Sciences (Grant No. XDB07020100).

Table I. Structural parameters of YSn_2 determined by single crystal XRD measurements at 293(2) K. Space group: $Cmc2_1$ (No. 36). Lattice parameters: a = 4.332(1) Å, b = 16.052(3) Å, c = 4.235(1) Å, $\alpha = \beta = \gamma = 90^{\circ}$. R_1 = 0.0611; wR_2 = 0.1291; Goodness of fit= 0.936. U_{eq} is defined as one-third of the trace of the orthogonalized U_{ij} tensor (Å^2).

Atom	Wyckoff.	Occupancy.	x	y	z	U_{eq}
Y	4*a*	0.94(2)	0	0.0999(4)	0.240(4)	0.016(2)
Sn1	4*a*	1	0	0.4372(3)	0.237(3)	0.024(1)
Sn2	4*a*	1	0	0.7490(3)	0.238(3)	0.023(1)

Table II. Parameters derived from the analyses of dHvA oscillations for YSn_2. F, oscillation frequency; T_D, Dingle temperature; m^*, effective mass; μ_q, quantum mobility; ϕ_B, Berry phase; δ, the phase shift factor in quantum oscillations; $\delta = 0$ for a 2D FS, but $\pm 1/8$ for a 3D FS (see text).

Field Direction	***F*(T)**	**Notation**	***T*$_D$(K)**	***m**/*m*$_0$**	***μ*$_q$ (cm^2/Vs)**	***ϕ*$_B$**
B*//*b′	23	F_α	95	0.029±0.002	776	0.968π±0.003 (δ=-1/8)
	301	F_γ	\	0.023±0.002	\	\
	433	F_θ	\	0.038±0.004	\	\
B*//*b **(Magnetization)**	78	F_β	10	0.082±0.002	2609	0.98π ±0.012 (δ=0)
B*//*ac′	21	F_α	60	0.022±0.002	1621	0.87π ±0.069 (δ=1/8)
	386	F_γ	82	0.034±0.003	767	0.49π ±0.032 (δ=-1/8)
	465	F_θ	60	0.065±0.008	891	0.66π ±0.019 (δ=1/8) or 1.16π ±0.019 (δ=-1/8)
	655	$F_\square$	\	0.040±0.003	\	\

Table III. Fermi wave vector and effective mass obtained from the first-principle calculations and dHvA experiments for the α-, β-, γ- and θ-pockets.

Pocket Name	dHvA frequencies (T) for $B//b'$	k_F (Å^{-1}) estimated from the dHvA	DFT-calculated k_F (Å^{-1})	Effective mass estimated from the dHvA (m_0)	DFT-calculated effective mass (m_0)
α	23	0.0264	0.025	0.029±0.002	0.0118
β	78	0.0478	\	0.082±0.002	\
γ	301	0.0955	0.09	0.023±0.002	0.0121
θ	433	0.115	0.111	0.038±0.004	0.0625

References:

[1] T. Liang, Q. Gibson, M. N. Ali, M. Liu, R. J. Cava, and N. P. Ong, Nat. Mater. **14**, 280 (2015).

[2] Y. Zhao, H. Liu, C. Zhang, H. Wang, J. Wang, Z. Lin, Y. Xing, H. Lu, J. Liu, Y. Wang, S. M. Brombosz, Z. Xiao, S. Jia, X. C. Xie, and J. Wang, Phys. Rev. X **5**, 031037 (2015).

[3] X. Huang, L. Zhao, Y. Long, P. Wang, D. Chen, Z. Yang, H. Liang, M. Xue, H. Weng, Z. Fang, X. Dai, and G. Chen, Phys. Rev. X **5**, 031023 (2015).

[4] Z. Wang, Y. Sun, X.-Q. Chen, C. Franchini, G. Xu, H. Weng, X. Dai, and Z. Fang, Phys. Rev. B **85**, 195320 (2012).

[5] H. Weng, C. Fang, Z. Fang, B. A. Bernevig, and X. Dai, Phys. Rev. X **5**, 011029 (2015).

[6] Z. K. Liu, J. Jiang, B. Zhou, Z. J. Wang, Y. Zhang, H. M. Weng, D. Prabhakaran, S. K. Mo, H. Peng, P. Dudin, and others, Nat. Mater. **13**, 677 (2014).

[7] S. Borisenko, Q. Gibson, D. Evtushinsky, V. Zabolotnyy, B. Büchner, and R. J. Cava, Phys. Rev. Lett. **113**, 027603 (2014).

[8] M. Neupane, S.-Y. Xu, R. Sankar, N. Alidoust, G. Bian, C. Liu, I. Belopolski, T.-R. Chang, H.-T. Jeng, H. Lin, A. Bansil, F. Chou, and M. Z. Hasan, Nat. Commun. **5**, 3786 (2014).

[9] S.-M. Huang, S.-Y. Xu, I. Belopolski, C.-C. Lee, G. Chang, B. Wang, N. Alidoust, G. Bian, M. Neupane, C. Zhang, S. Jia, A. Bansil, H. Lin, and M. Z. Hasan, Nat. Commun. **6**, 7373 (2015).

[10] H. Weng, C. Fang, Z. Fang, B. A. Bernevig, and X. Dai, Phys. Rev. X **5**, 011029 (2015).

[11] F. Arnold, C. Shekhar, S.-C. Wu, Y. Sun, R. D. dos Reis, N. Kumar, M. Naumann, M. O. Ajeesh, M. Schmidt, A. G. Grushin, J. H. Bardarson, M. Baenitz, D. Sokolov, H. Borrmann, M. Nicklas, C. Felser, E. Hassinger, and B. Yan, Nat. Commun. **7**, 11615 (2016).

[12] L. X. Yang, Z. K. Liu, Y. Sun, H. Peng, H. F. Yang, T. Zhang, B. Zhou, Y. Zhang, Y. F. Guo, M. Rahn, D. Prabhakaran, Z. Hussain, S.-K. Mo, C. Felser, B. Yan, and Y. L. Chen, Nat. Phys. **11**, 728 (2015).

[13] B. Q. Lv, H. M. Weng, B. B. Fu, X. P. Wang, H. Miao, J. Ma, P. Richard, X. C. Huang, L. X. Zhao, G. F. Chen, Z. Fang, X. Dai, T. Qian, and H. Ding, Phys. Rev. X **5**, 031013 (2015).

[14] C. Shekhar, A. K. Nayak, Y. Sun, M. Schmidt, M. Nicklas, I. Leermakers, U. Zeitler, Y. Skourski, J. Wosnitza, Z. Liu, Y. Chen, W. Schnelle, H. Borrmann, Y. Grin, C. Felser, and B. Yan, Nat. Phys. **11**, 645 (2015).

[15] I. Belopolski, S.-Y. Xu, D. S. Sanchez, G. Chang, C. Guo, M. Neupane, H. Zheng, C.-C. Lee, S.-M. Huang, G. Bian, N. Alidoust, T.-R. Chang, B. Wang, X. Zhang, A. Bansil, H.-T. Jeng, H. Lin, S. Jia, and M. Z. Hasan, Phys. Rev. Lett. **116**, 066802 (2016).

[16] S.-Y. Xu, N. Alidoust, I. Belopolski, Z. Yuan, G. Bian, T.-R. Chang, H. Zheng, V. N. Strocov, D. S. Sanchez, G. Chang, C. Zhang, D. Mou, Y. Wu, L. Huang, C.-C. Lee, S.-M. Huang, B. Wang, A. Bansil, H.-T. Jeng, T. Neupert, A. Kaminski, H. Lin, S. Jia, and M. Zahid Hasan, Nat. Phys. **11**, 748 (2015).

[17] L. Lu, Z. Wang, D. Ye, L. Ran, L. Fu, J. D. Joannopoulos, and M. Soljačić, Science **349**, 622 (2015).

[18] T. Zhang, Z. Song, A. Alexandradinata, H. Weng, C. Fang, L. Lu, and Z. Fang, Phys. Rev. Lett. **120**, 016401 (2018).

[19] X. Wan, A. M. Turner, A. Vishwanath, and S. Y. Savrasov, Phys. Rev. B **83**, 205101 (2011).
[20] G. Xu, H. Weng, Z. Wang, X. Dai, and Z. Fang, Phys. Rev. Lett. **107**, 186806 (2011).
[21] S. Borisenko, D. Evtushinsky, Q. Gibson, A. Yaresko, T. Kim, M. N. Ali, B. Buechner, M. Hoesch, and R. J. Cava, arXiv:150704847 (2015).
[22] Z. Wang, M. G. Vergniory, S. Kushwaha, M. Hirschberger, E. V. Chulkov, A. Ernst, N. P. Ong, R. J. Cava, and B. A. Bernevig, Phys. Rev. Lett. **117**, 236401 (2016).
[23] G. Chang, S.-Y. Xu, H. Zheng, B. Singh, C.-H. Hsu, G. Bian, N. Alidoust, I. Belopolski, D. S. Sanchez, S. Zhang, H. Lin, and M. Z. Hasan, Sci. Rep. **6**, 38839 (2016).
[24] A. A. Soluyanov, D. Gresch, Z. Wang, Q. Wu, M. Troyer, X. Dai, and B. A. Bernevig, Nature **527**, 495 (2015).
[25] Y. Wu, D. Mou, N. H. Jo, K. Sun, L. Huang, S. L. Bud'ko, P. C. Canfield, and A. Kaminski, Phys. Rev. B **94**, 121113 (2016).
[26] Y. Sun, S.-C. Wu, M. N. Ali, C. Felser, and B. Yan, Phys. Rev. B **92**, 161107 (2015).
[27] K. Deng, G. Wan, P. Deng, K. Zhang, S. Ding, E. Wang, M. Yan, H. Huang, H. Zhang, Z. Xu, J. Denlinger, A. Fedorov, H. Yang, W. Duan, H. Yao, Y. Wu, S. Fan, H. Zhang, X. Chen, and S. Zhou, Nat. Phys. **12**, 1105 (2016).
[28] S.-Y. Xu, N. Alidoust, G. Chang, H. Lu, B. Singh, I. Belopolski, D. S. Sanchez, X. Zhang, G. Bian, H. Zheng, M.-A. Husanu, Y. Bian, S.-M. Huang, C.-H. Hsu, T.-R. Chang, H.-T. Jeng, A. Bansil, T. Neupert, V. N. Strocov, H. Lin, S. Jia, and M. Z. Hasan, Sci. Adv. **3**, e1603266 (2017).
[29] K. Koepernik, D. Kasinathan, D. V. Efremov, S. Khim, S. Borisenko, B. Büchner, and J. van den Brink, Phys. Rev. B **93**, 201101 (2016).
[30] S. Khim, K. Koepernik, D. V. Efremov, J. Klotz, T. Förster, J. Wosnitza, M. I. Sturza, S. Wurmehl, C. Hess, J. van den Brink, and B. Büchner, Phys. Rev. B **94**, 165145 (2016).
[31] E. Haubold, K. Koepernik, D. Efremov, S. Khim, A. Fedorov, Y. Kushnirenko, J. van den Brink, S. Wurmehl, B. Büchner, T. K. Kim, M. Hoesch, K. Sumida, K. Taguchi, T. Yoshikawa, A. Kimura, T. Okuda, and S. V. Borisenko, Phys. Rev. B **95**, 241108 (2017).
[32] X. Zhou, Q. Liu, Q. Wu, T. Nummy, H. Li, J. Griffith, S. Parham, J. Waugh, E. Emmanouilidou, B. Shen, O. V. Yazyev, N. Ni, and D. Dessau, arXiv:170910245 (2017).
[33] J. Park, G. Lee, F. Wolff-Fabris, Y. Y. Koh, M. J. Eom, Y. K. Kim, M. A. Farhan, Y. J. Jo, C. Kim, J. H. Shim, and others, Phys. Rev. Lett. **107**, 126402 (2011).
[34] Y. Feng, Z. Wang, C. Chen, Y. Shi, Z. Xie, H. Yi, A. Liang, S. He, J. He, Y. Peng, X. Liu, Y. Liu, L. Zhao, G. Liu, X. Dong, J. Zhang, C. Chen, Z. Xu, X. Dai, Z. Fang, and X. J. Zhou, Sci. Rep. **4**, 5385 (2014).
[35] K. Wang, D. Graf, L. Wang, H. Lei, S. W. Tozer, C. Petrovic, and others, Phys. Rev. B **85**, 041101 (2012).
[36] G. Lee, M. A. Farhan, J. S. Kim, and J. H. Shim, Phys. Rev. B **87**, 245104 (2013).
[37] J. B. He, Y. Fu, L. X. Zhao, H. Liang, D. Chen, Y. M. Leng, X. M. Wang, J. Li, S. Zhang, M. Q. Xue, C. H. Li, P. Zhang, Z. A. Ren, and G. F. Chen, Phys. Rev. B **95**, 045128 (2017).
[38] J. Y. Liu, J. Hu, Q. Zhang, D. Graf, H. B. Cao, S. M. A. Radmanesh, D. J. Adams, Y. L. Zhu, G. F. Cheng, X. Liu, W. A. Phelan, J. Wei, M. Jaime, F. Balakirev, D. A. Tennant, J. F. DiTusa, I. Chiorescu, L. Spinu, and Z. Q. Mao, Nat. Mater. **16**, 905 (2017).
[39] J. Liu, J. Hu, H. Cao, Y. Zhu, A. Chuang, D. Graf, D. J. Adams, S. M. A. Radmanesh, L. Spinu, I. Chiorescu, and Z. Mao, Sci. Rep. **6**, 30525 (2016).
[40] Y.-Y. Wang, S. Xu, L.-L. Sun, and T.-L. Xia, Phys. Rev. Mater. **2**, 021201 (2018).

[41] M. A. Farhan, G. Lee, and J. H. Shim, J. Phys. Condens. Matter **26**, 042201 (2014).
[42] C. Yi, S. Yang, M. Yang, L. Wang, Y. Matsushita, S. Miao, Y. Jiao, J. Cheng, Y. Li, K. Yamaura, Y. Shi, and J. Luo, Phys. Rev. B **96**, 205103 (2017).
[43] Q. Xu, Z. Song, S. Nie, H. Weng, Z. Fang, and X. Dai, Phys. Rev. B **92**, 205310 (2015).
[44] L. M. Schoop, M. N. Ali, C. Stra\s ser, A. Topp, A. Varykhalov, D. Marchenko, V. Duppel, S. S. Parkin, B. V. Lotsch, and C. R. Ast, Nat. Commun. **7**, 11696 (2016).
[45] N. Kumar, K. Manna, Y. Qi, S.-C. Wu, L. Wang, B. Yan, C. Felser, and C. Shekhar, Phys. Rev. B **95**, 121109 (2017).
[46] J. Hu, Z. Tang, J. Liu, X. Liu, Y. Zhu, D. Graf, K. Myhro, S. Tran, C. N. Lau, J. Wei, and Z. Mao, Phys. Rev. Lett. **117**, 016602 (2016).
[47] J. Hu, Y. L. Zhu, D. Graf, Z. J. Tang, J. Y. Liu, and Z. Q. Mao, Phys. Rev. B **95**, 205134 (2017).
[48] L. M. Schoop, A. Topp, J. Lippmann, F. Orlandi, L. Müchler, M. G. Vergniory, Y. Sun, A. W. Rost, V. Duppel, M. Krivenkov, S. Sheoran, P. Manuel, A. Varykhalov, B. Yan, R. K. Kremer, C. R. Ast, and B. V. Lotsch, Sci. Adv. **4**, 2317 (2018).
[49] M. M. Hosen, G. Dhakal, K. Dimitri, P. Maldonado, A. Aperis, F. Kabir, P. M. Oppeneer, D. Kaczorowski, T. Durakiewicz, and M. Neupane, arXiv:170705292 (2017).
[50] R. Singha, A. Pariari, B. Satpati, and P. Mandal, Phys. Rev. B **96**, 245138 (2017).
[51] J. Hu, Y. Zhu, D. Graf, Z. Tang, and Z. Mao, arXiv:171005403 (2017).
[52] R. Lou, J.-Z. Ma, Q.-N. Xu, B.-B. Fu, L.-Y. Kong, Y.-G. Shi, P. Richard, H.-M. Weng, Z. Fang, S.-S. Sun, Q. Wang, H.-C. Lei, T. Qian, H. Ding, and S.-C. Wang, Phys. Rev. B **93**, 241104 (2016).
[53] M. Neupane, I. Belopolski, M. M. Hosen, D. S. Sanchez, R. Sankar, M. Szlawska, S.-Y. Xu, K. Dimitri, N. Dhakal, P. Maldonado, P. M. Oppeneer, D. Kaczorowski, F. Chou, M. Z. Hasan, and T. Durakiewicz, Phys. Rev. B **93**, 201104 (2016).
[54] SHELXTL, version 6.10, Bruker AXS Inc.: Madison, WI, 2000.
[55] Sheldrick, G. M. Acta Crystallogr. A 2008, 64, 112.
[56] P. Hohenberg and W. Kohn, Phys. Rev. **136**, B864 (1964).
[57] W. Kohn and L. J. Sham, Phys. Rev. **140**, A1133 (1965).
[58] J. P. Perdew, K. Burke, and M. Ernzerhof, Phys. Rev. Lett. **77**, 3865 (1996).
[59] J. P. Perdew, K. Burke, and M. Ernzerhof, Phys. Rev. Lett. **78**, 1396 (1997).
[60] G. Kresse and J. Furthmüller, Phys. Rev. B **54**, 11169 (1996).
[61] G. Kresse and J. Furthmüller, Comput. Mater. Sci. **6**, 15 (1996).
[62] H. J. Monkhorst and J. D. Pack, Phys. Rev. B **13**, 5188 (1976).
[63] N. Marzari and D. Vanderbilt, Phys. Rev. B **56**, 12847 (1997).
[64] I. Souza, N. Marzari, and D. Vanderbilt, Phys. Rev. B **65**, 035109 (2001).
[65] Yue Cheng-Yang, Chin. J. Inorg. Chem. **11**, 025 (2011).
[66] L. L. Zhao, M. S. Mehlman, T. Besara, T. Siegrist, and E. Morosan, J. Magn. Magn. Mater. **341**, 6 (2013).
[67] I. M. Lifshitz and A. M. Kosevich, Sov Phys JETP **2**, 636 (1956).
[68] D. Shoenberg, *Magnetic Oscillations in Metals*, Cambridge University Press (2009).
[69] G. P. Mikitik and Y. V. Sharlai, Phys. Rev. Lett. **82**, 2147 (1999).
[70] J. Hu, J. Y. Liu, D. Graf, S. M. A. Radmanesh, D. J. Adams, A. Chuang, Y. Wang, I. Chiorescu, J. Wei, L. Spinu, and Z. Q. Mao, Sci. Rep. **6**, 18674 (2016).
[71] J. Hu, Z. Tang, J. Liu, Y. Zhu, J. Wei, and Z. Mao, Phys. Rev. B **96**, 045127 (2017).

[72] B. A. Bernevig and T. L. Hughes, *Topological Insulators and Topological Superconductors,* Princeton University Press (2013).
[73] H. Murakawa, M. S. Bahramy, M. Tokunaga, Y. Kohama, C. Bell, Y. Kaneko, N. Nagaosa, H. Y. Hwang, and Y. Tokura, Science **342**, 1490 (2013).

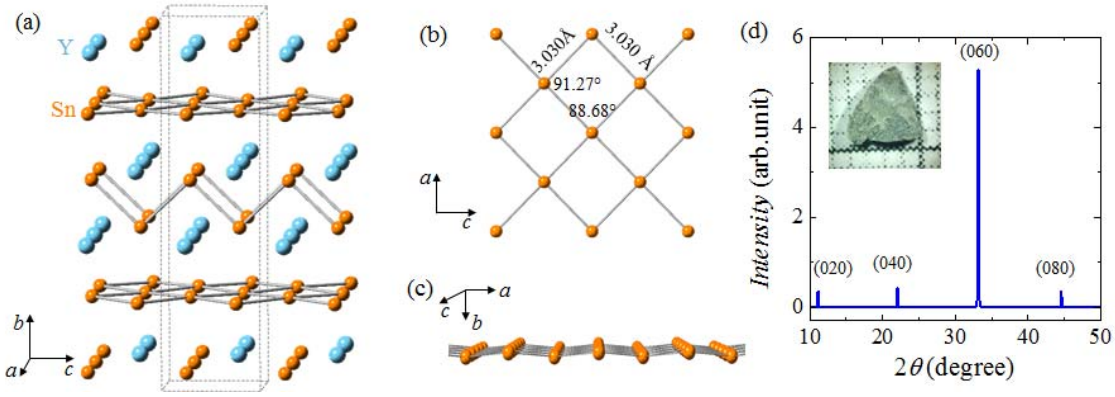

Figure 1: (a) Crystal structure of YSn_2. (b) Top view of Sn plane. (c) Distorted Sn layer of YSn_2 (d) Single crystal X-ray diffraction spectra of YSn_2. Inset is an optical image of single crystal YSn_2.

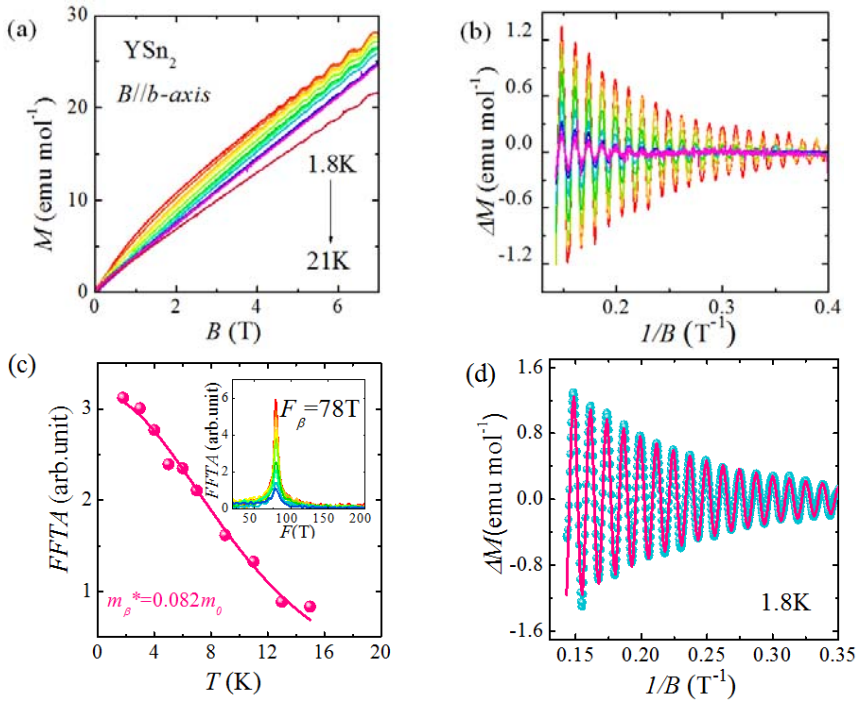

Figure 2. (a) Isothermal out-of plane ($B//b$ axis) magnetization M for YSn_2 at various temperatures (T=1.8K to 21K). (b) Oscillatory magnetization after subtracting the background for $B//b$ in the 1.8-21K temperature range. (c) The fits of the FFT amplitudes of the dHvA oscillations to the temperature damping factor R_T in the LK formula. Inset shows the FFT spectra of the oscillatory magnetization for $B//b$. (d) The fit of the dHvA oscillation pattern at 1.8K by the LK formula, with the solid line representing the fitted curve.

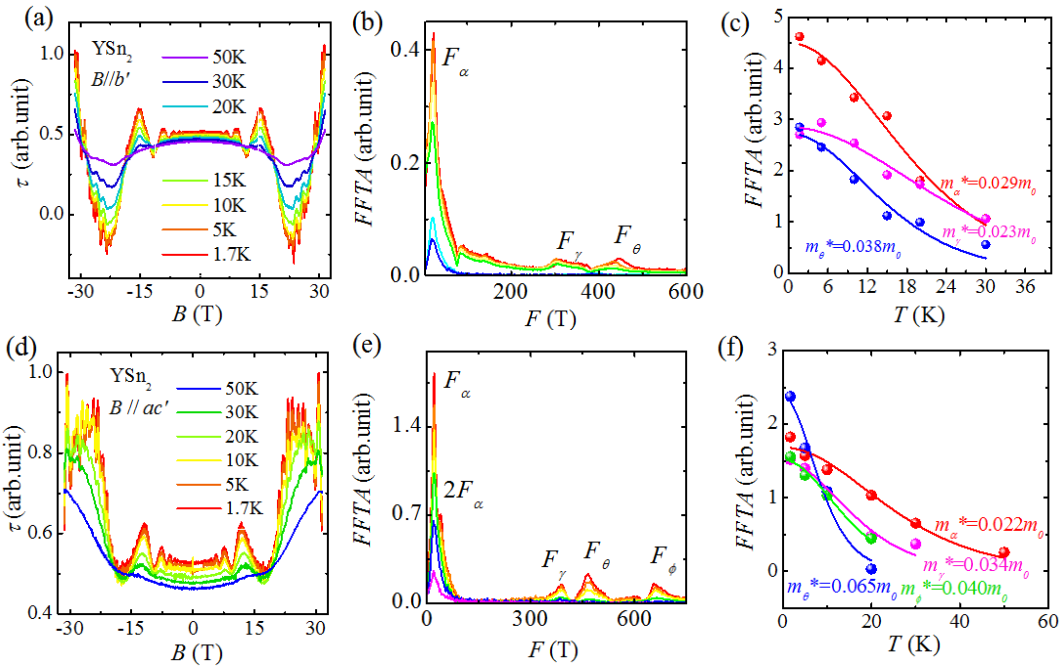

Figure 3. (a) and (d): The field dependence of magnetic torque τ for YSn_2 at different temperatures from 1.7K to 50K, which show strong dHvA oscillations. The magnetic field is applied nearly along the *b*-axis (a) and *ac* plane (d). (b) and (e) show the FFT spectra of the oscillatory magnetization $\Delta\tau$ for $B//b'$ and $B//ac'$ respectively. (c) and (f) show the fits of the FFT amplitudes by the temperature damping term R_T of the LK formula.

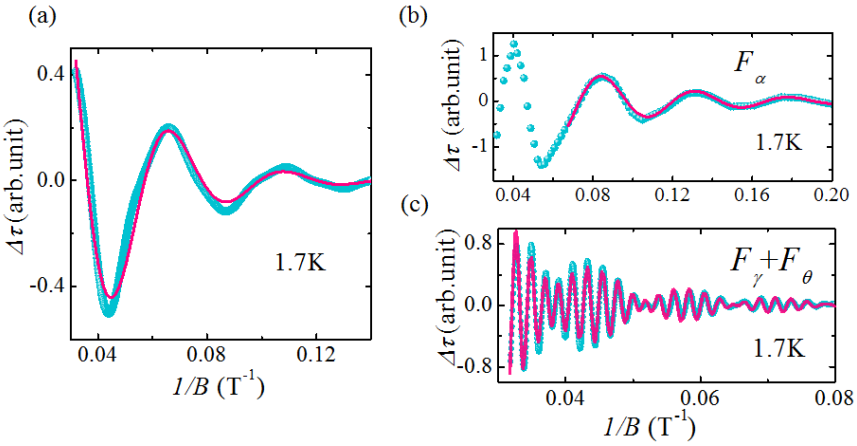

Figure 4. (a) and (b) show the low frequency (F_α) dHvA oscillations probed in magnetic torque for $B//b'$ and $B//ac'$ respectively, obtained after filtering the high-frequency components. (c) shows the high frequency (F_γ and F_θ) oscillatory components of magnetic torque for $B//ac'$, obtained after filtering the low-frequency components. The solid curves in (a), (b) and (c) represent the fits of the T=1.7K oscillation patterns by the single/two-band LK formula.

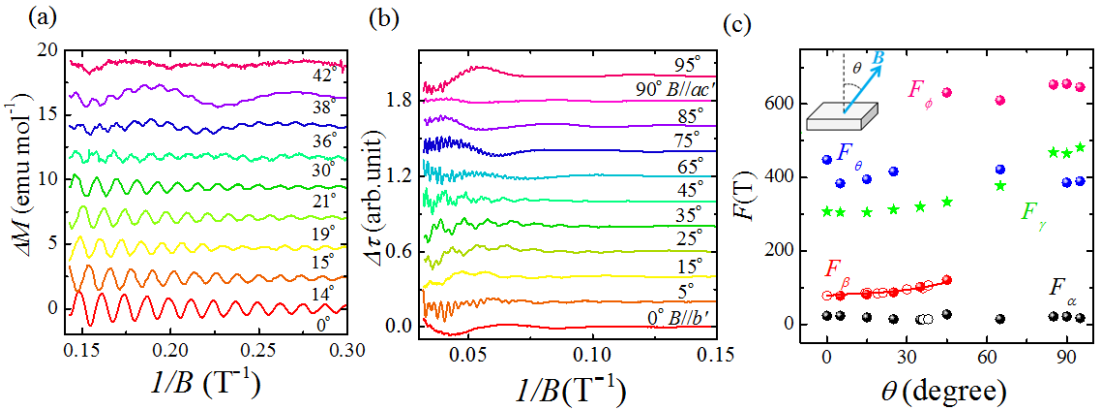

Figure 5. (a) dHvA oscillations of isothermal magnetization (M) for YSn_2 at T=1.8K under different magnetic field orientations. (b) dHvA oscillations of magnetic torque of YSn_2 at T=1.8K under different magnetic field orientations. The data of different θ have been shifted for clarity and the non-oscillating background has been subtracted. (c) The angular dependences of oscillation frequencies for YSn_2. Inset: the experimental setup.

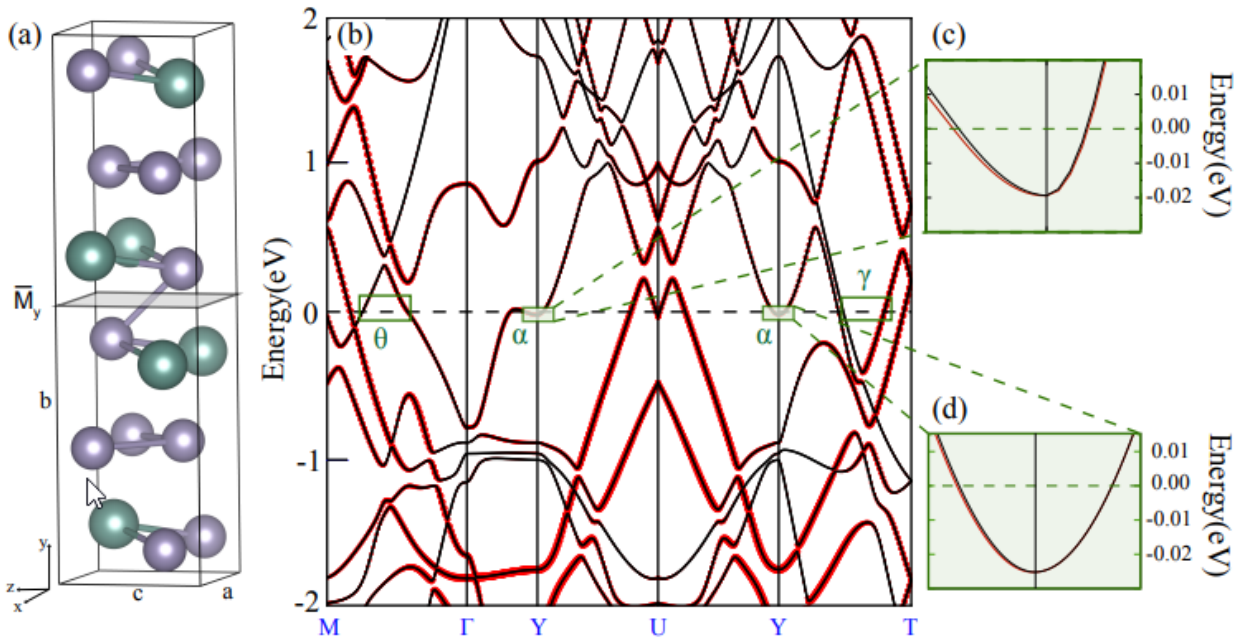

Figure 6. (a) Crystal structure for YSn_2 with the space group of *Cmc2₁*. There is a distorted Sn-lattice every two layers and a glide mirror $\bar{M}_y\left\{\frac{1}{2},\frac{1}{2},0\right\}$ for YSn_2. (b) Band dispersions for YSn_2. The radius of red dots represents atomic projections from Sn in the Sn-lattice. (c-d) Magnified band dispersion of the α pocket along different directions. The two bands are non-degenerated along Γ-Y and Y-U directions and form a nodal line along the Y-T direction.

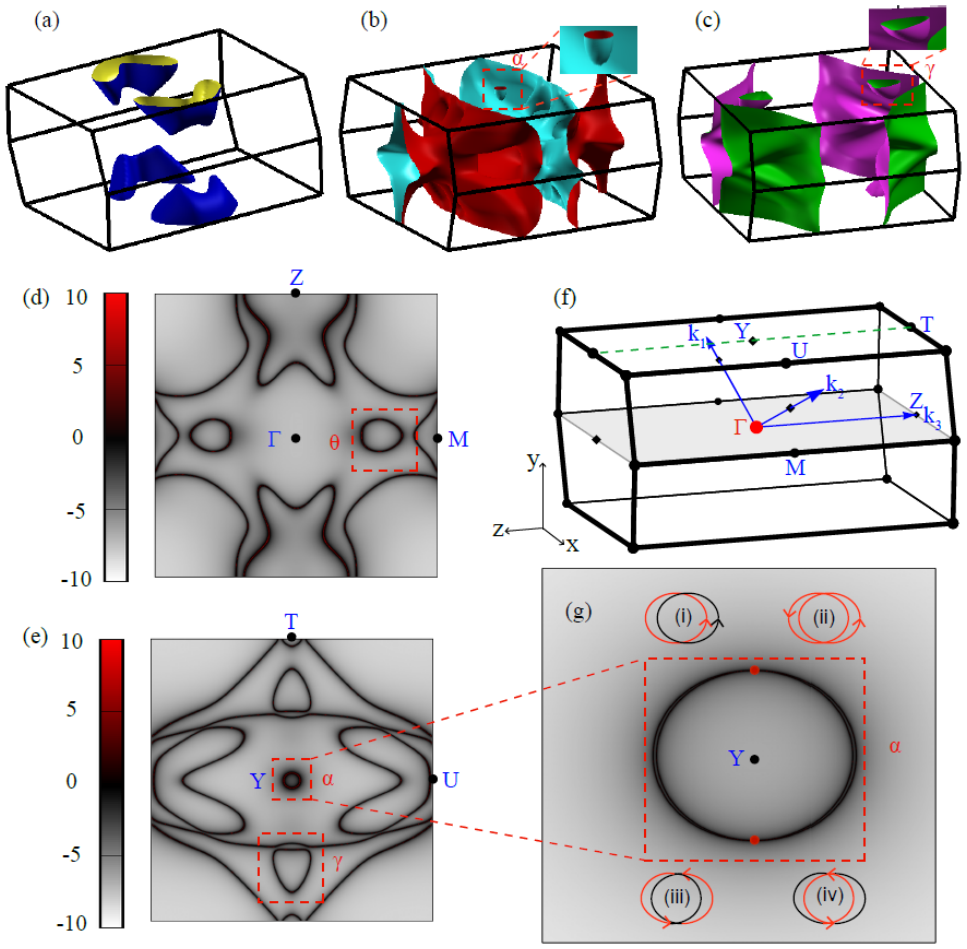

Figure 7. (a-c) shows the Fermi surface formed by the three pairs of bands around Fermi level. (d-e) shows the Fermi surfaces for YSn_2 at $k_y = 0$ and $k_y = \pi$ plane respectively. (f) is the BZ for YSn_2 and the green dashed line indicates the momenta of nodal line. (g) shows the magnification of the α-pocket where the two red points are two crossing points along the T-Y direction. (i), (ii), (ii) and (iv) in (g) depict four possible paths of cyclotron orbitals for the Fermi pocket α for $B//b$.